Dual-Functional RhNi Nanocubes Coupling the Electrocatalytic Water Reduction and Alcohol Oxidation for Energy-Saving Hydrogen Production

Hui-Zi Huang,[a] Di Liu,[a,b] Zhejiaji Zhu,[a] Wenjing Tian,[a] Li-Wei Chen,[a] Jiani Li,[a] and An-Xiang Yin *[a]

[a] *Ministry of Education Key Laboratory of Cluster Science, Beijing Key Laboratory of Photoelectronic/Electrophotonic Conversion Materials, Advanced Technology Research Institute (Jinan), School of Chemistry and Chemical Engineering, Beijing Institute of Technology, Beijing 100081, P. R. China.*

[b] *Department of Pharmaceutical Engineering, School of Life and Health Sciences, Huzhou College, Huzhou 313000, P. R. China.*

* To whom correspondence should be addressed: yin@bit.edu.cn

1. Experimental section

1.1 Chemicals and materials

Rhodium acetylacetonate [$Rh(acac)_3$, 99.99%, Alfa Aesar, USA], nickel acetylacetonate [$Ni(acac)_2$, 97%, Aladdin, China], oleylamine (OAm, 80–90%, Aladdin, China), cetyltrimethylammonium bromide (CTAB, 99%, Aladdin, China), *L*-ascorbic acid (AA, 99%, Aladdin, China), carbon black (CB, Vulcan XC-72R, 99.9%, Carbot Co., USA), commercial Pt on carbon black (20% Pt/C, Alfa Aesar, USA), potassium hydroxide (KOH, 99.99%, Aladdin, China), ethanol (EtOH, 99.9%, Aladdin, China), ethylene glycol (EG, 99%, Alfa Aesar, USA), deuterated water (D_2O, 99.9%, Aladdin, China), dimethyl sulfoxide (DMSO, ≥ 99.8%, Aladdin, China), Nafion solution (5 wt% in methanol and H_2O, DuPont, USA), tetradecyl trimethyl ammonium bromide (TTAB, 99%, Meryer, China), and polyvinyl pyrrolidone (PVP, MW = 24000, Aladdin, China) were used as received without further purification. The ultrapure water (18.2 MΩ cm) used in all experiments was prepared by passing deionized water through an ultra-pure purification system (Milli-Q).

1.2 Preparation of Rh-based electrocatalysts

In a typical synthesis of Rh–Ni nanocubes (RhNi NCs), 0.02 mmol (5.14 mg) of $Ni(acac)_2$, 0.04 mmol (14.6 mg) of CTAB, and 5 mL of OAm were added into a 50 mL three-necked flask. The solution was heated to 120 °C, kept for 30 min to obtain a homogeneous solution, and then further quickly heated to 250 °C under N_2 atmosphere. Then, Rh stock solution prepared by dissolving 0.04 mmol (16.0 mg) of $Rh(acac)_3$ and 0.08 mmol (14.0 mg) of AA in 1 mL of OAm at 60 °C was rapidly injected into the hot solution. The reaction mixture was kept at 250 °C for another 60 min and gradually turned black. Finally, the reaction mixture was cooled down to room temperature naturally, centrifuged, and washed by cyclohexane and ethanol three times. The as-obtained RhNi NCs were redispersed in cyclohexane to form a stable colloidal dispersion.

The synthesis of Rh–Ni nanospheres (RhNi NSs) followed the similar procedures of RhNi NCs except that no AA was added.

Rh nanoparticles (Rh NPs) were synthesized through a solvothermal method for comparison. Typically, 0.1 mmol of $RhCl_3 \cdot 3H_2O$, 0.5 mmol of tetradecyl trimethyl ammonium bromide (TTAB), and 2 mmol of PVP (MW = 24000) were dissolved into 20 mL of EG solution and heated at 80 °C for 20 min to obtain a brown homogeneous solution. Then, the solution was heated at 185 °C for 1.5 h, the reaction product was centrifuged and then washed several times by plenty of ethanol and acetone. The as-obtained Rh NPs were redispersed in ethanol to further use.

1.3 Loading electrocatalysts on carbon supports

The high surface area Vulcan XC-72R carbon black was dispersed in cyclohexane and then sonicated in an ice bath for 30 min to ensure the formation of homogeneous suspension. Subsequently, the as-prepared colloidal dispersion of Rh-based catalysts were added dropwise to the carbon cyclohexane dispersion. The catalysts were further sonicated for 40 min in an ice bath and stirred for another 300 min. The resulting carbon-supported catalysts were collected by filtration and then dried in the oven, followed by calcination in the air atmosphere at 250 °C for 2 h to remove the surfactant. The mass loading of metals in the CB-supported catalysts was measured by inductively coupled plasma-optical emission spectroscopy (ICP-OES).

1.4 Characterization

The X-ray diffraction (XRD) patterns were recorded on a Rigaku MiniFlex 600 diffractometer with a Cu K_α X-ray radiation source ($\lambda = 0.154056$ nm) at a scan rate of $10°\cdot min^{-1}$. The transmission electron microscopy (TEM) images were conducted by a JEOL JEM-2100 transmission electron microscope. High-resolution TEM (HRTEM), energy-dispersive spectrometer (EDS), high angle annular dark-field scanning transmission electron microscopy (HAADF-STEM), and mapping/line-scanning were performed on a Talos F200X transmission electron microscope. The aberration-corrected high-angle annular dark-field scanning transmission electron microscopy (AC-HAADF-STEM) studies were obtained using an FEI Themis Z with double aberration correctors. The X-ray photoelectron spectroscopy (XPS) spectra were carried out on a Thermo Fisher ESCALAB 250 Xi XPS system with a monochromatic Al K_α X-ray source. ^{1}H nuclear magnetic resonance (NMR) spectra were performed on a Bruker Ascend 400 (400 MHz) spectrometer. ICP-OES studies were performed on an Agilent ICP-OES 720 spectrometer. *In situ* Fourier transform infrared spectroscopy (FTIR) experiments were conducted on a Nicolet iS50 FTIR spectrometer equipped with an MCT detector cooled with liquid nitrogen. The spectral resolution was set to 8 cm^{-1}, and 64 interferograms were co-added for each spectrum. A reference spectrum was acquired at 0.10 V vs. RHE. The sample spectra were recorded during the chronopotentiometry tests with the anodic potential increased from 0.2 to 1.1 V vs. RHE in the step of 0.10 V. All gas chromatography (GC) experiments were performed on an online GC-2014C (SHIMADZU, Japan).

1.5 Electrode preparation and electrochemical measurements in three-electrode system

General electrochemical hydrogen evolution reaction (HER) and ethanol oxidation reaction (EOR) were carried out in a three-electrode system. A platinum plate (1×1 cm^2) and a saturated calomel electrode (SCE) were used as the counter electrode and reference electrode, respectively. Electrochemical measurements were conducted on an electrochemical workstation (CHI 660E, China) at room temperature. All potentials were measured against the SCE and converted to the reversible hydrogen electrode (RHE) reference scale.

To prepare working electrodes, 1 mg of the CB-supported catalyst powder and 10 μL of 5 wt% Nafion solution were dispersed in the mixture of 700 μL of ethanol and 290 μL of H_2O to form a homogeneous ink after 0.5 h of sonication in ice bath. Then the prepared ink was quantitatively dropped onto glassy carbon electrode (5 mm in diameter, PINE instruments) and used as the working electrode.

The HER measurements were conducted in 1.0 M KOH solution. The linear sweep voltammetry (LSV) measurements for HER were carried out at 5 mV s^{-1} with 95% iR compensation. The Tafel slopes were obtained from the LSV curves. The electrochemical impedance spectroscopy (EIS) of the samples for HER was recorded with AC voltage at –0.017 V vs. RHE from 0.1 Hz to 10^5 Hz in 1.0 M KOH. The chronopotentiometry test for HER was performed at a current density of 10 mA cm^{-2}.

The EOR performance were tested in (0.1 M KOH + 1.0 M EtOH) solution during 0 ~ 1.087 V at 50 mV s^{-1}. The EIS for EOR was recorded with AC voltage at 0.750 V vs. RHE from 0.1 Hz to 10^5 Hz in the mixture of 0.1 M KOH and 1.0 M EtOH. The chronoamperometric test for EOR was carried out at 0.6 V vs. RHE.

1.6 Electrode preparation and electrochemical measurements in two-electrode system

The two-electrode H-type cell was constructed for the coupled HER/EOR electrocatalysis using 1.0 M KOH as catholyte and (1.0 M KOH + 1.0 M EtOH) solution as anolyte. To prepare working electrodes, 4 mg of the CB-supported catalyst powder and 10 μL of 5 wt% Nafion solution were dispersed in the mixture of 280 μL of ethanol and 110 μL of H_2O to form a homogeneous ink after 0.5 h of sonication at room temperature. Then the prepared ink was quantitatively loaded onto a 1 × 1 cm^2 carbon paper dropwise to achieve a mass loading of 0.1 mg_{Rh} cm^{-2} and used as the anode and cathode electrodes. The scanning rate of the LSV curves were 5 mV s^{-1}. The chronopotentiometry test for the coupled HER/EOR was performed at a current density of 10 mA cm^{-2} and 50 mA cm^{-2}.

The configurations for coupling HER with the methanol oxidation reaction (HER || MOR), glycerol oxidation reaction (HER || GOR), and ethylene glycol oxidation reaction (HER || EGOR) were similar to the HER || EOR, except for using different alcohols (*i.e.*, methanol, glycerol, and ethylene glycol).

1.7 Product analysis

The liquid products were characterized by ^{1}H NMR spectra. Typically, 1 mL of D_2O and 10 μL of DMSO were mixed to obtain solution A, then 55 μL of solution A was measured and diluted with 2.3 mL of D_2O to prepare an internal standard solution (250 ppm). 500 μL of the extracted electrolyte after electrolysis was mixed with 100 μL of internal standard solution.

The Faradaic efficiency (*FE*) value of each product was calculated by dividing the charge consumption for corresponding product with the total charge passing through the circuit during the electrolysis reaction. The *FE* of CH_3COO^- was calculated from the equation below:

$$FE_{\text{liquid}}\,(\%) = V \times c \times \frac{nF}{Q}$$

where V is the volume of the electrolyte in the anodic cell (mL); c is the concentration of liquid product after electrolysis, determined by ^{1}H NMR (mol mL^{-1}); n is the number of transferred electrons for certain product (for CH_3COO^-, $n = 4$); F is the Faradaic constant (96485 C mol^{-1}); Q is the total charge consumed in the electrolysis (C).

The gaseous product (H_2) from the cathodic compartment during the electrolysis of coupled HER/EOR was collected and measured via the water displacement method. The H_2 was also quantitatively analyzed by GC, using N_2 as the carrier gas. Their *FE* was calculated as follows:

$$FE_{H_2}\,(\%) = C \times V \times \frac{nFP}{RTi}$$

where C is the concentration of the gas product (H_2) measured by GC (ppm), V is the flow rate of N_2 (mL min^{-1}), n is the number of transferred electrons for certain product (for H_2, $n = 2$), F is the Faradaic constant (96485 C mol^{-1}), P is the ambient pressure ($P = 101.325$ KPa), T is the room temperature ($T = 298$ K), R is the gas constant (R = 8.314 J mol^{-1} K^{-1}), and i is the total current during a constant-current electrolysis ($i = 10$ mA).

1.8 DFT calculations

Density functional theory (DFT) calculations were performed in the Vienna ab initio simulation package (VASP). A spin-polarized generalized gradient approximation (GGA) Perdew-Burke-Ernzerhof (PBE) functional was adopted to calculate the exchange-correlation interaction.[1,2] The projector augmented wave (PAW) method with a cutoff energy of 400 eV was used for the plane wave basis, and 3 × 3 × 1 (for {100}) and 3 × 2 × 1 (for {111}) Γ-centered k-mesh in the Brillouin zone were applied for the k-pace integration.[3,4] A climbing image nudged elastic band (CI-NEB) method implemented in VASP was used to locate the transition states for reaction energy barrier simulation.[5]

The Gibbs free energy change (ΔG) for adsorptions was calculated by the following equation:

$$\Delta G = \Delta E + \Delta E_{\text{ZPE}} - T\Delta S$$

where ΔE_{ZPE} is the zero-point energy change, ΔS is the entropy change, and T is temperature at 298.15 K.

2. Supplementary Figures

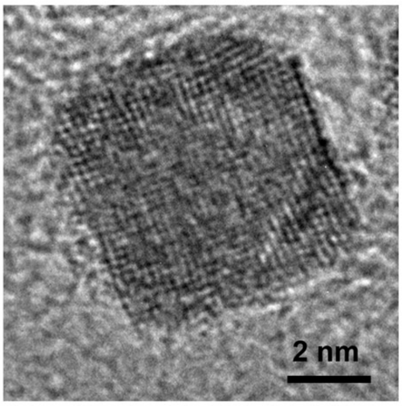

Fig. S1. HRTEM image of one RhNi NC.

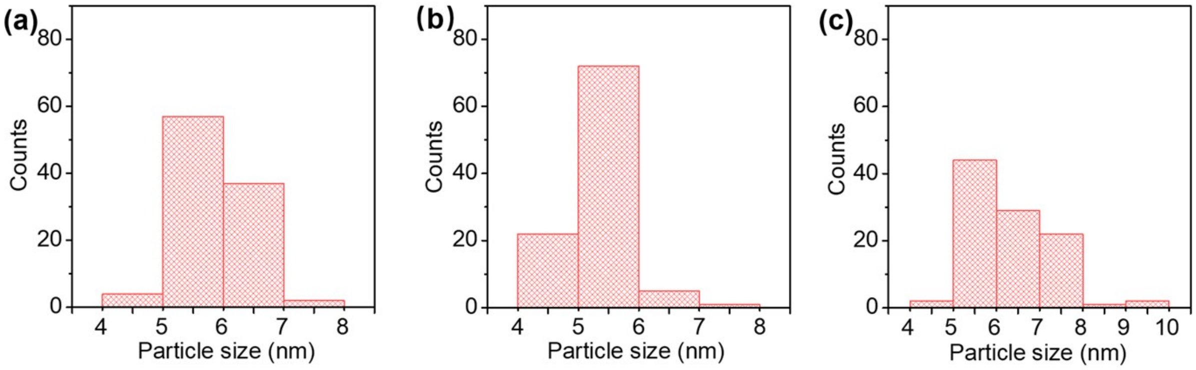

Fig. S2. The histograms of particle size distributions. (a) RhNi NCs, (b) RhNi NSs, and (c) Rh NPs.

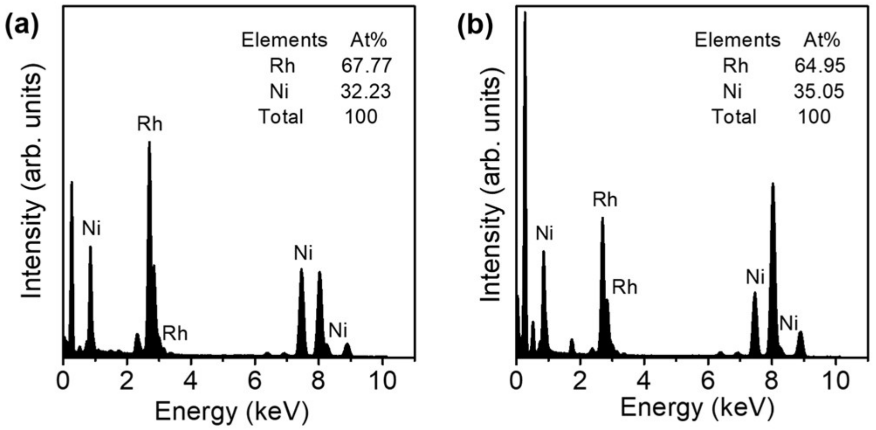

Fig. S3. Elemental analysis by EDS. (a) RhNi NCs and (b) RhNi NSs.

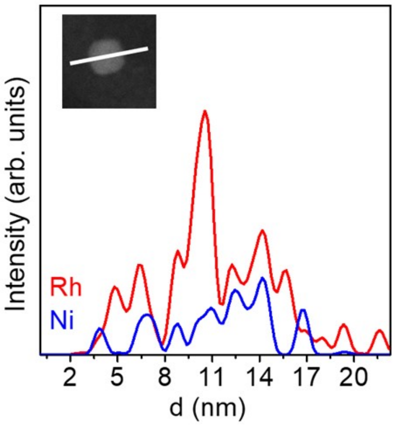

Fig. S4. HAADF-STEM image and corresponding EDS line scanning profile of one RhNi NC.

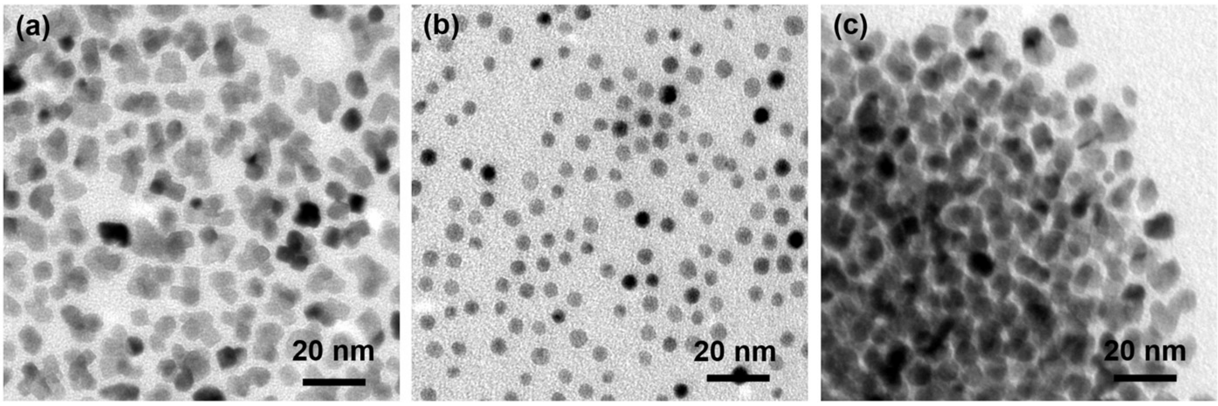

Fig. S5. TEM images of the RhNi nanocrystals synthesized by using different amounts of CTAB or KBr. (a) 0.01 mmol of CTAB, (b) 0.16 mmol of CTAB, and (c) 0.08 mmol of KBr.

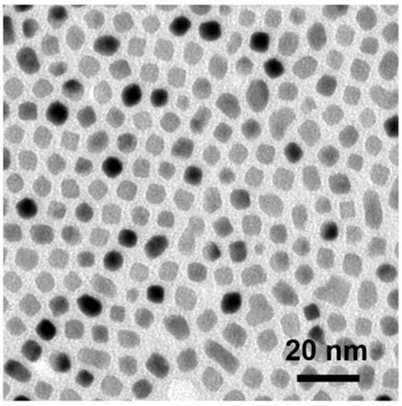

Fig. S6. TEM image of the RhNi nanocrystals synthesized by using 0.16 mmol of AA.

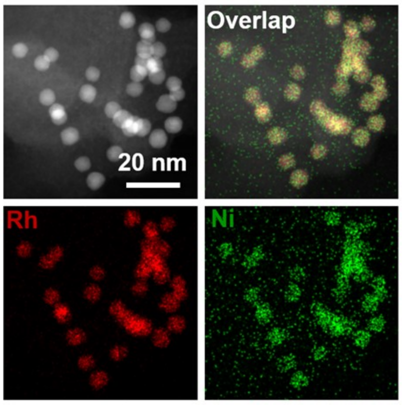

Fig. S7. HAADF-STEM image and the corresponding EDS elemental mapping of RhNi NSs.

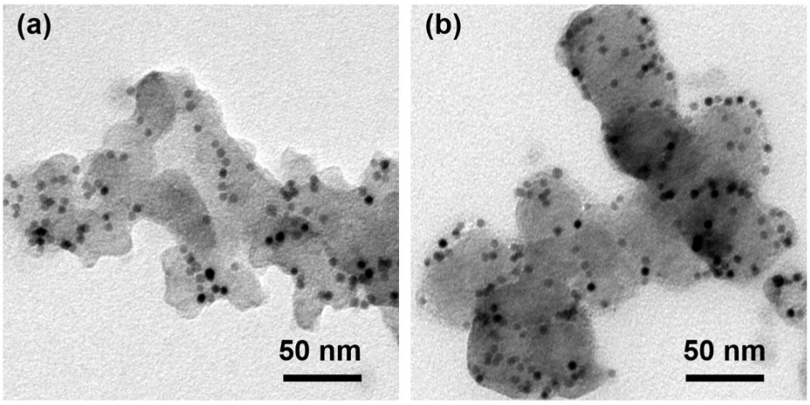

Fig. S8. TEM images of Rh NPs supported on carbon black.

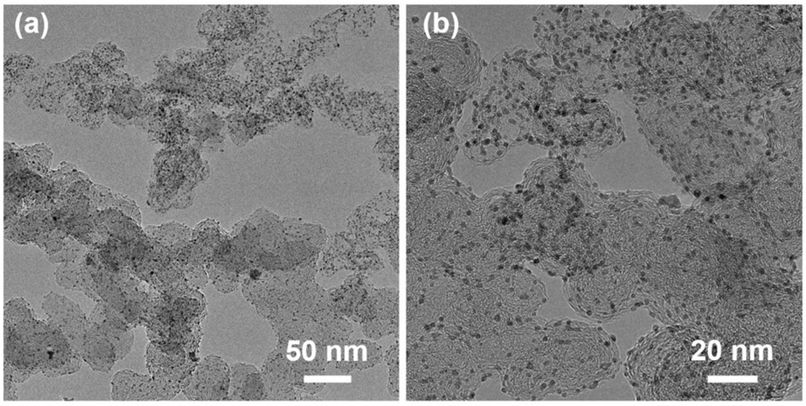

Fig. S9. TEM images of the commercial Pt/C.

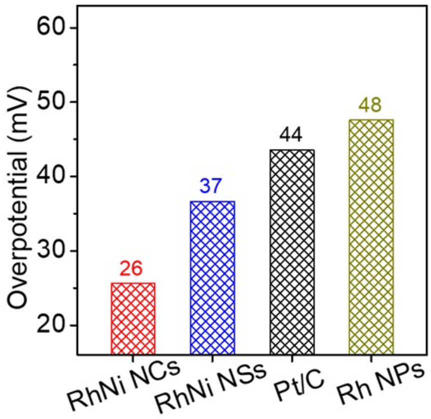

Fig. S10. Overpotentials for HER (at 10 mA cm^{-2}) on RhNi NCs, RhNi NSs, Rh NPs, and commercial Pt/C.

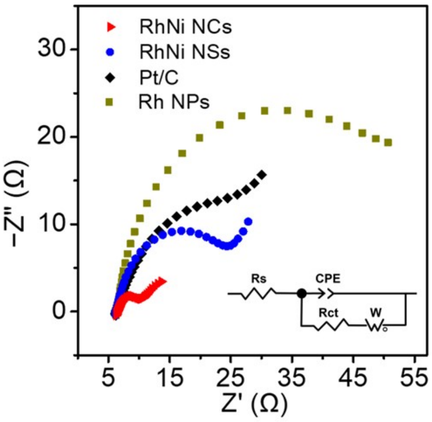

Fig. S11. Nyquist plots of RhNi NCs, RhNi NSs, Rh NPs, and commercial Pt/C in 1.0 M KOH.

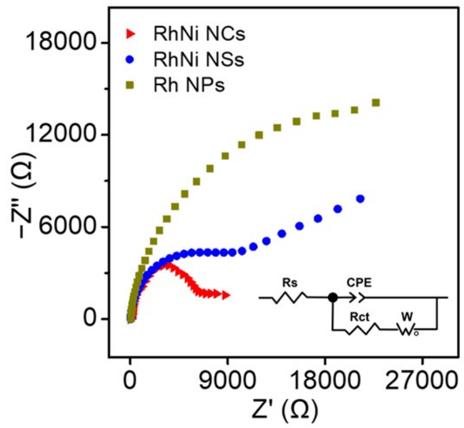

Fig. S12. Nyquist plots of RhNi NCs, RhNi NSs, and Rh NPs in the solution of 0.1 M KOH + 1.0 M C_2H_5OH.

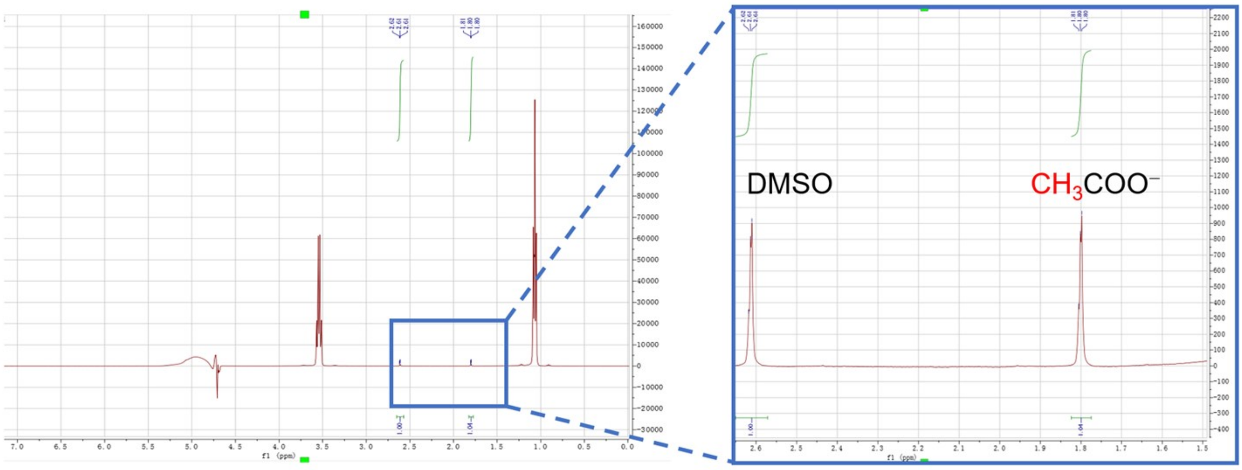

Fig. S13. The typical ^{1}H NMR profile of the residual electrolyte after 10000 s of EOR on RhNi NCs.

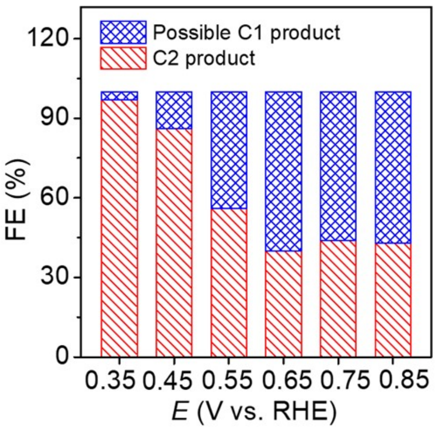

Fig. S14. FE for electrocatalytic products of EOR on RhNi NCs at different potentials.

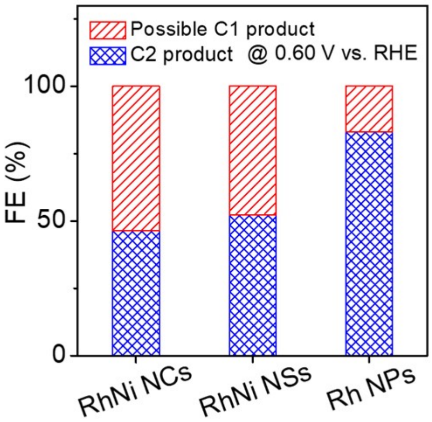

Fig. S15. FE of possible C1 and C2 products for EOR on RhNi NCs, RhNi NSs, and Rh NPs at 0.6 V vs. RHE.

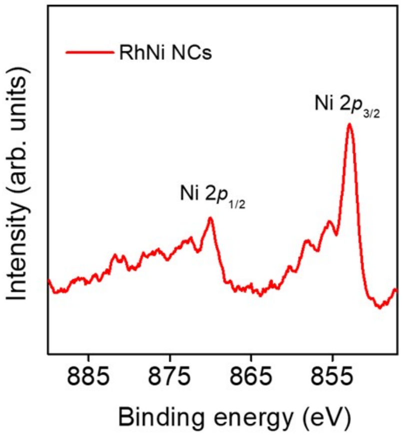

Fig. S16. Ni 2*p* XPS spectra of RhNi NCs.

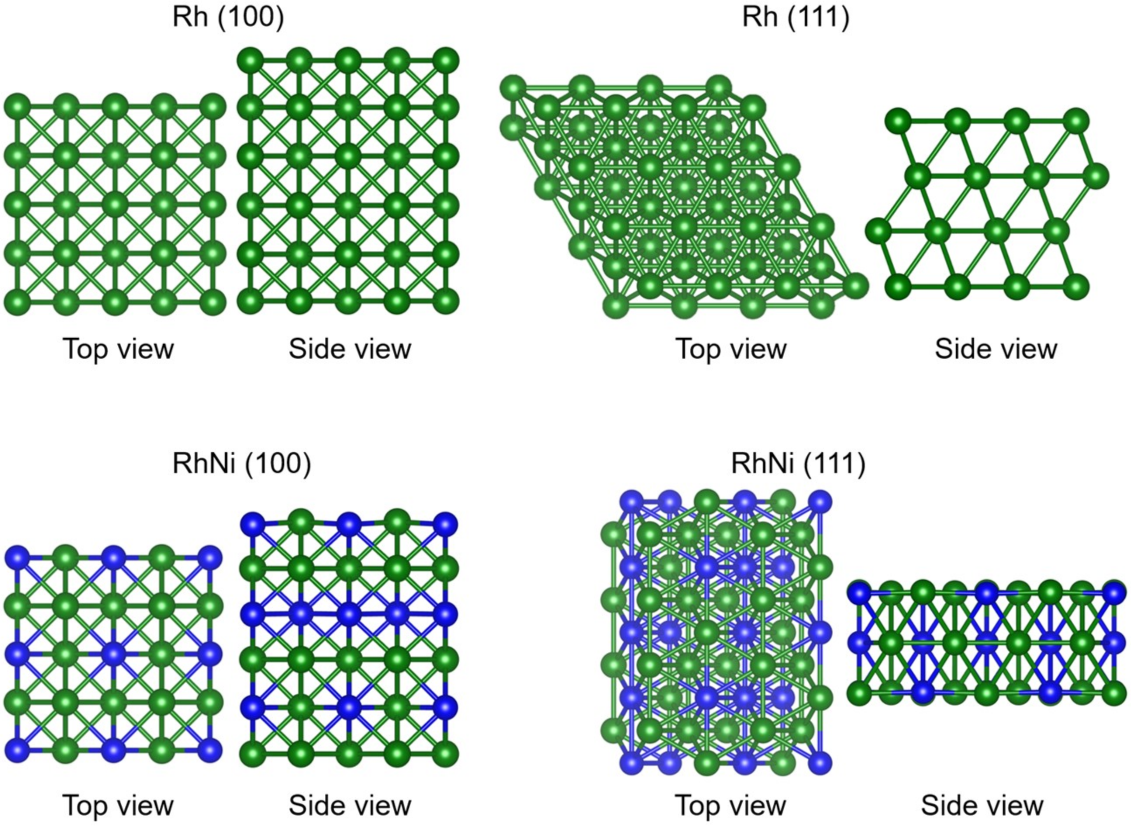

Fig. S17. Crystal structure models of Rh (100), Rh (111), RhNi (100), and Rh (111).

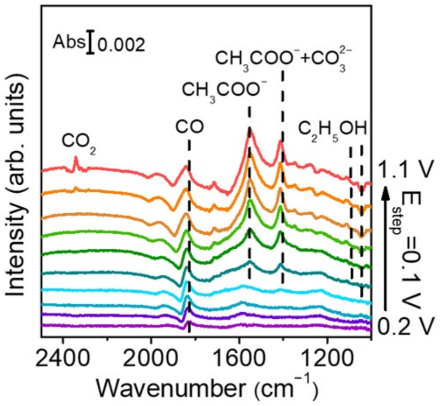

Fig. S18. *In situ* FTIR for EOR on RhNi NSs in the mixed electrolytes of 0.1 M KOH and 1.0 M EtOH at different potentials varying from 0.2 to 1.1 V vs. RHE with an interval of 0.1 V.

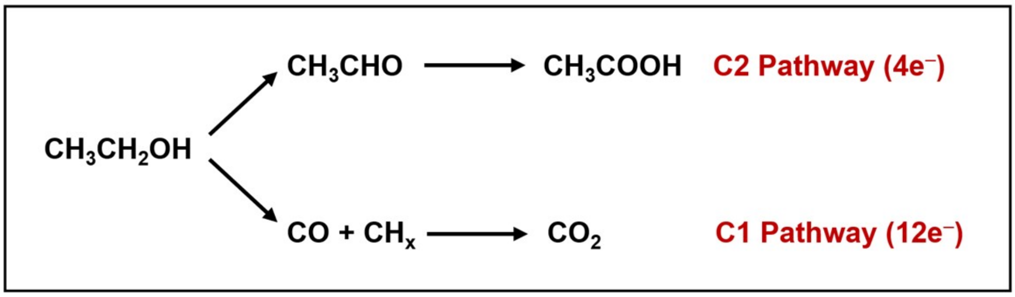

Fig. S19. Simplified schematic illustration for the dual-pathway mechanism of EOR.

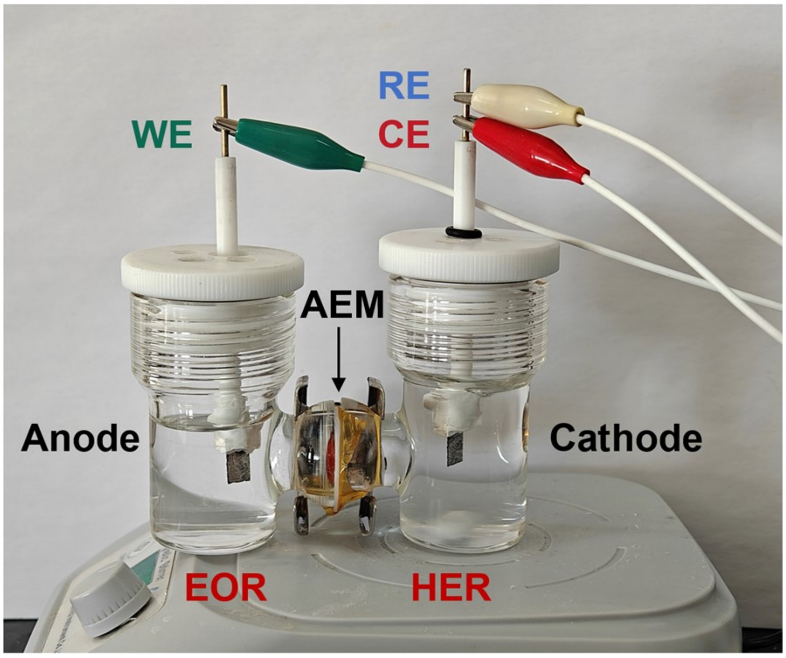

Fig. S20. Digital photograph of the two-electrode cell electrolyzer using RhNi NCs as both anodic and cathodic catalysts.

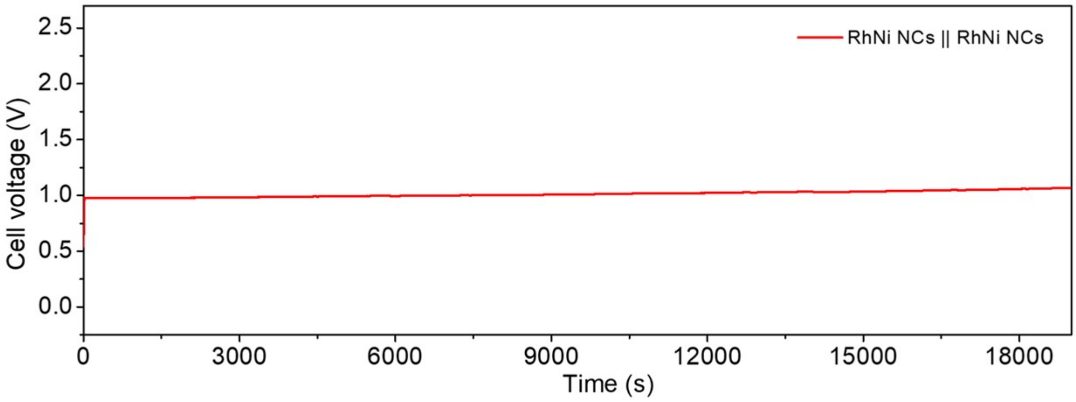

Fig. S21. The chronopotentiometry curves at 50 mA cm^{-2} for coupled HER and EOR with symmetric electrodes using RhNi NCs || RhNi NCs catalysts.

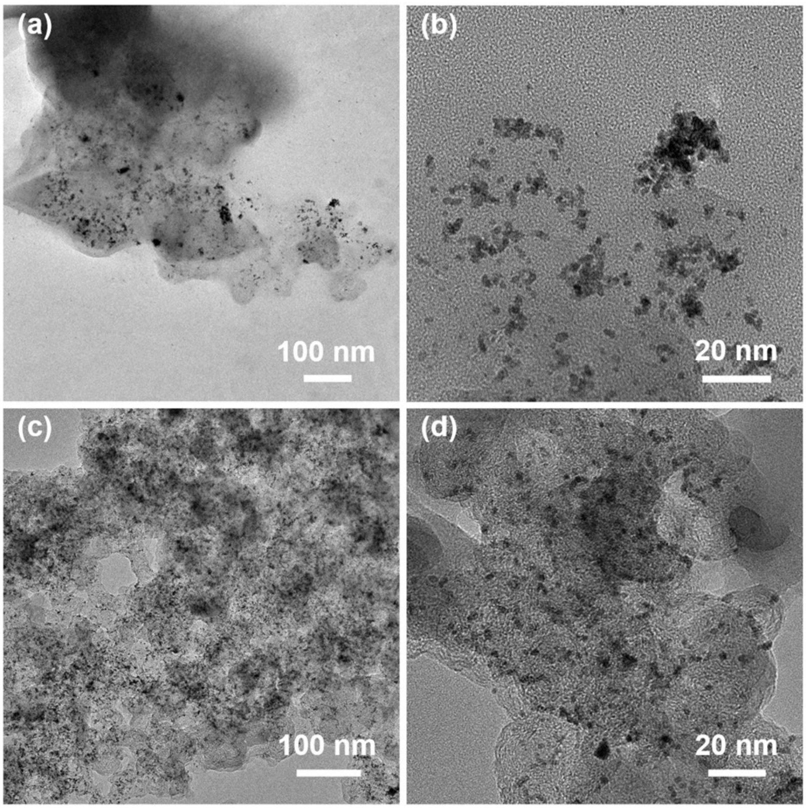

Fig. S22. TEM images of Pt/C after 8 hours of chronopotentiometry test for HER/EOR in (1.0 M KOH + 1.0 M C_2H_5OH) solution at (a,b) anode and (c,d) cathode.

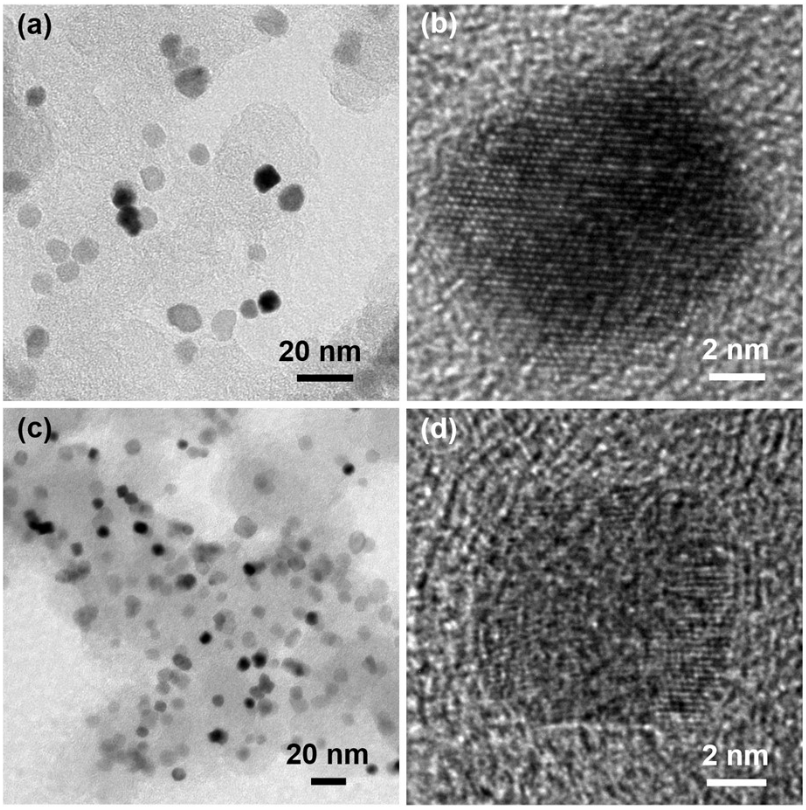

Fig. S23. TEM images of RhNi NCs after 8 hours of chronopotentiometry test for HER/EOR in (1.0 M KOH + 1.0 M C_2H_5OH) at (a,b) anode and (c,d) cathode.

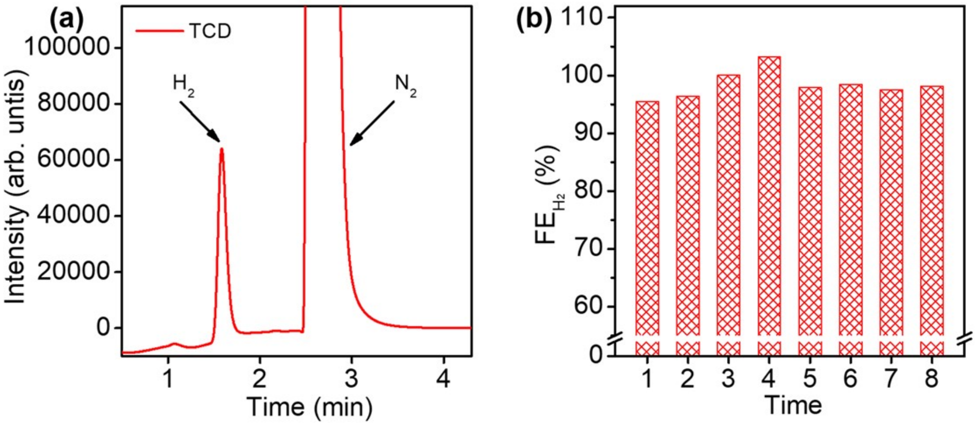

Fig. S24. Quantification of H_2 produced at the cathode in the coupled HER || EOR cell. (a) Representative GC profiles for the gaseous products during coupled HER/EOR electrolysis at 10 mA cm^{-2} and (b) the corresponding FE values for the generation of H_2 in the cathodic cell at different times on RhNi NCs.

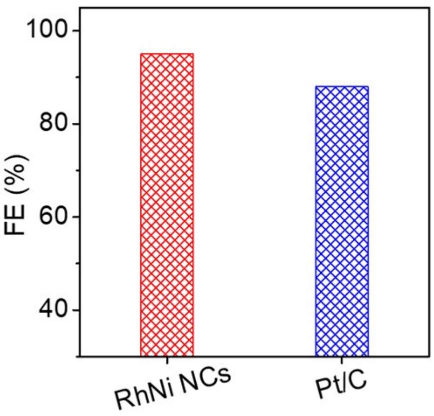

Fig. S25. FE of acetate product for HER/EOR in the anodic cell after 8 h amperometric i-t test on RhNi NCs and commercial Pt/C.

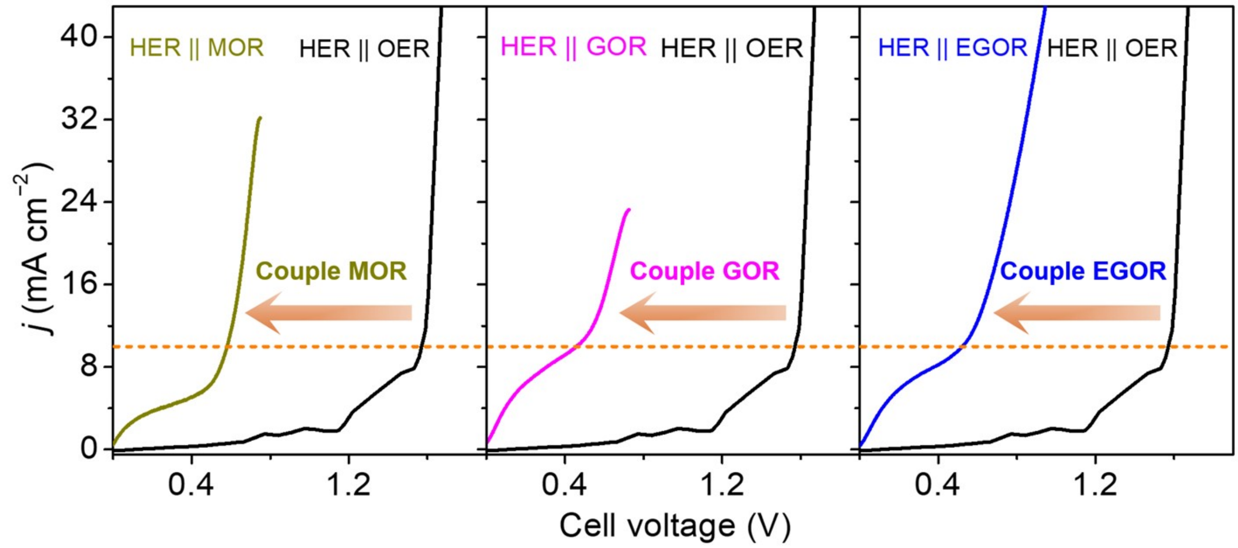

Fig. S26. LSV curves in the two-electrode cell electrolyzer using RhNi NCs as both cathodic and anodic catalysts for coupled HER and various alcohol oxidation tests (methanol, glycerol, and ethylene glycol) in 1.0 M KOH || (1.0 M KOH + 1.0 M alcohols) or for coupled HER and OER test in 1.0 M KOH || 1.0 M KOH.

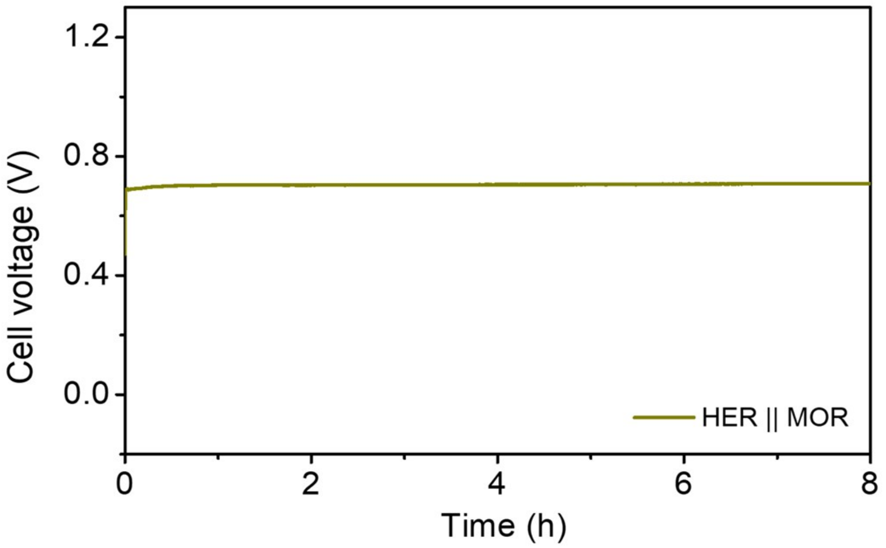

Fig. S27. The chronopotentiometry curves at 10 mA cm^{-2} for coupled HER and MOR with symmetric electrodes using RhNi NCs || RhNi NCs catalysts.

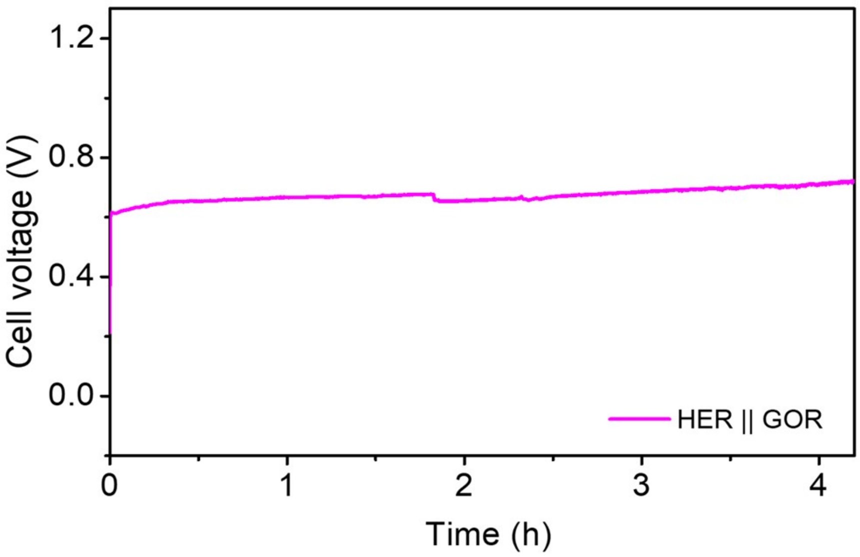

Fig. S28. The chronopotentiometry curve at 10 mA cm^{-2} for coupled HER and GOR with symmetric electrodes using RhNi NCs || RhNi NCs catalysts.

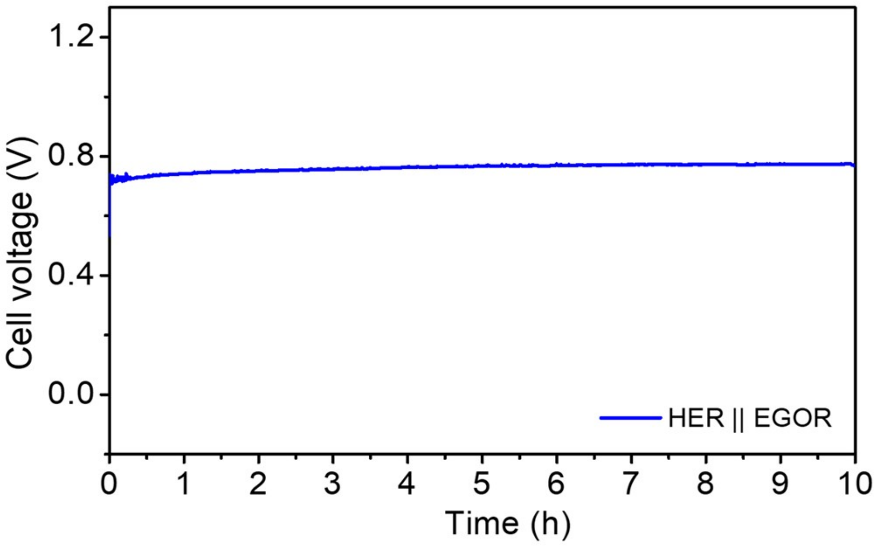

Fig. S29. The chronopotentiometry curve at 10 mA cm^{-2} for coupled HER and EGOR with symmetric electrodes using RhNi NCs || RhNi NCs catalysts.

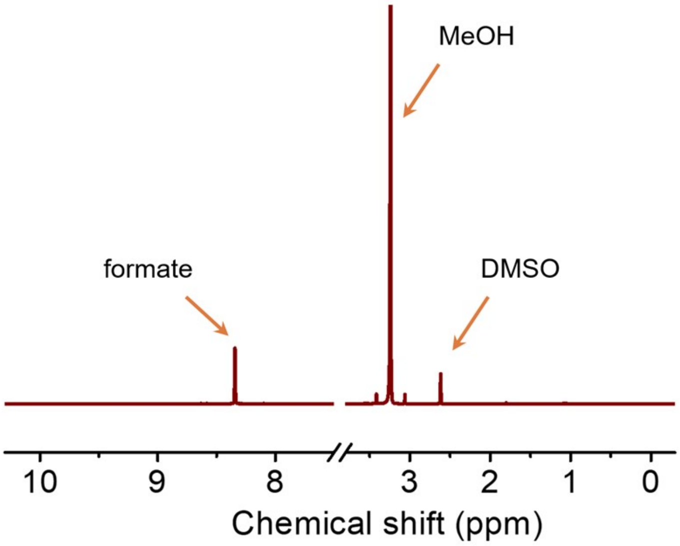

Fig. S30. ^{1}H NMR spectra of the anodic electrolyte after a 10-hour amperometric i-t test of HER || MOR on RhNi NCs electrode.

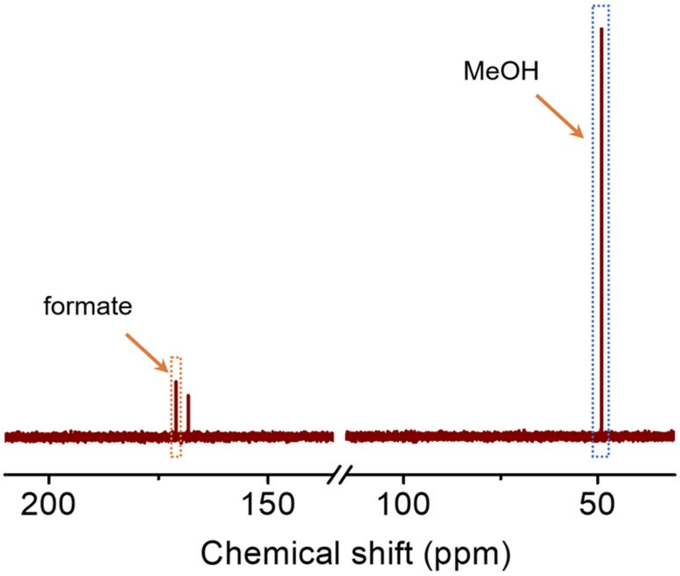

Fig. S31. ^{13}C NMR spectra of the anodic electrolyte after a 10-hour amperometric i-t test of HER || MOR on RhNi NCs electrode.

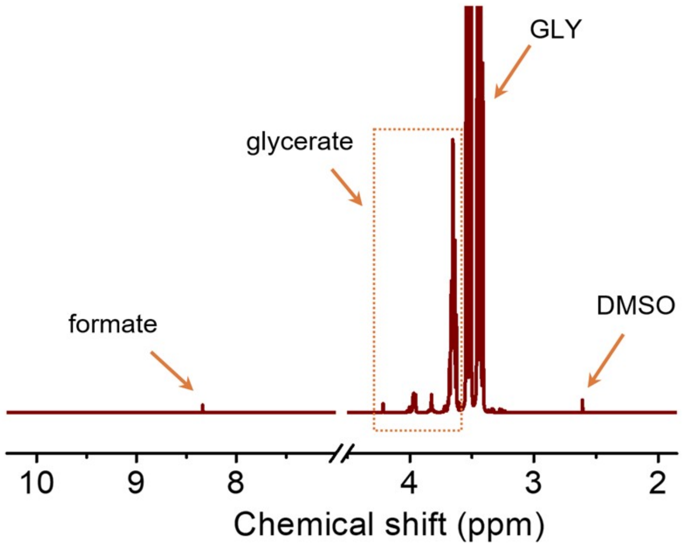

Fig. S32. ^{1}H NMR spectra of the anodic electrolyte after a 10-hour amperometric i-t test of HER || GOR on RhNi NCs electrode.

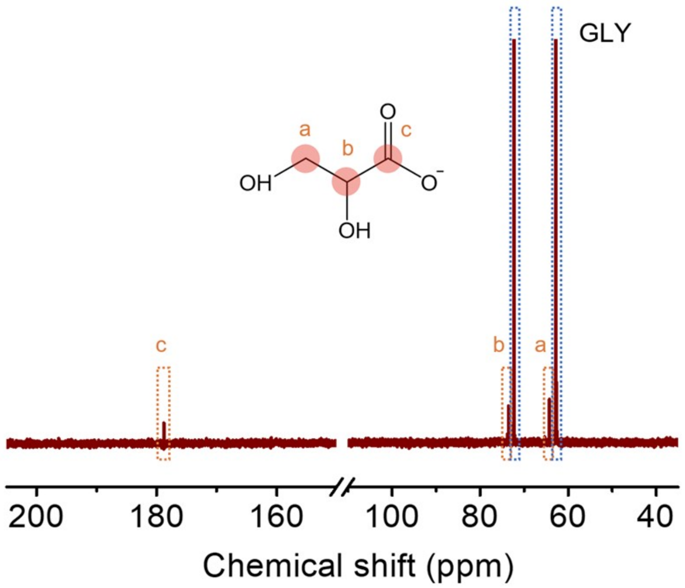

Fig. S33. ^{13}C NMR spectra of the anodic electrolyte after a 10-hour amperometric i-t test of HER || GOR on RhNi NCs electrode.

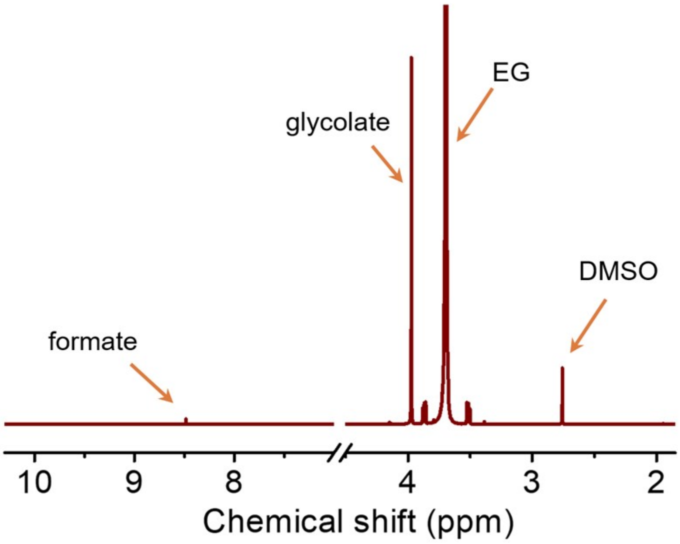

Fig. S34. ^{1}H NMR spectra of the anodic electrolyte after a 10-hour amperometric i-t test of HER || EGOR on RhNi NCs electrode.

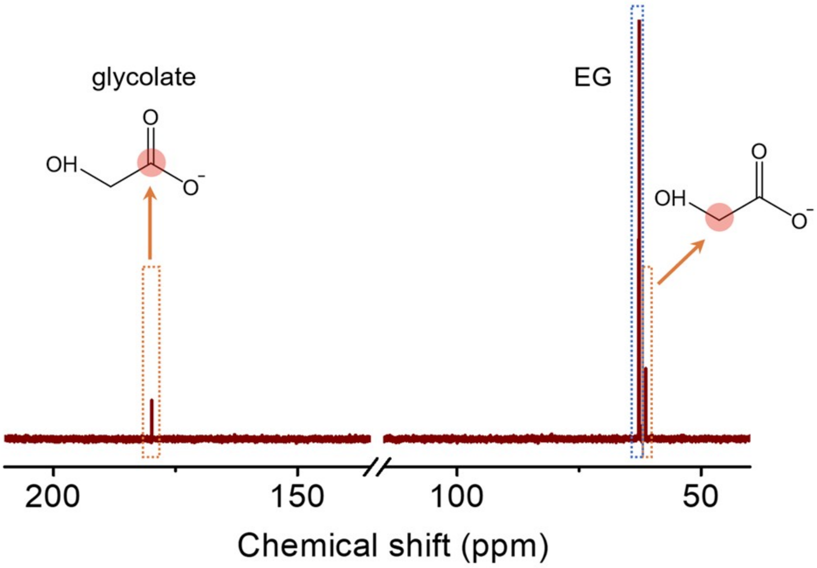

Fig. S35. ^{13}C NMR spectra of the anodic electrolyte after a 10-hour amperometric i-t test of HER || EGOR on RhNi NCs electrode.

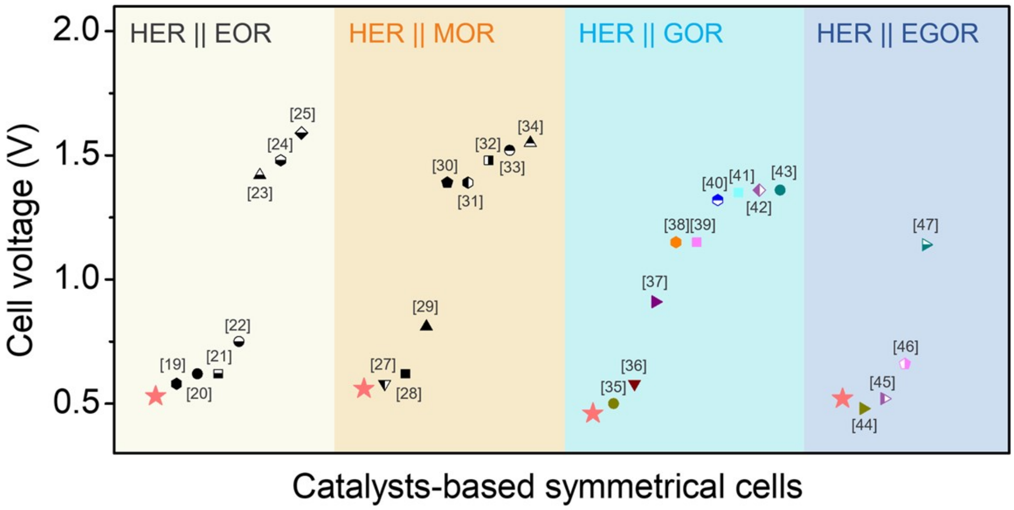

Fig. S36. Activity comparison of catalysts for energy-saving H_2 production at 10 mA cm^{-2}.

Table S1. Summary of the ECSAs, loading, specific activities, and mass activities at peak potential for Rh-based catalysts.

Catalysts	ECSA (cm^2)	Loading (μg_{Rh} cm^{-2})	Specific activity @ peak potential ($mA\ cm^{-2}{}_{(ECSA)}$)	Mass activity @ peak potential ($mA\ mg_{Rh}{}^{-1}$)
RhNi NCs	2.19	7.3	0.78	928.1
RhNi NSs	1.98	7.6	0.66	696.8
Rh NPs	2.28	11.2	0.41	408.5

Table S2. Comparison of activity of noble-metal-based catalysts for HER in alkaline electrolyte.

Catalysts	Electrolytes	Overpotentials of HER @ 10 mA cm^{-2}	References
RhNi NCs	1.0 M KOH	26 mV	This work
RhNi NSs	1.0 M KOH	37 mV	This work
Ni_3Sn_2-$NiSnO_x$-2	1.0 M KOH	14 mV	[6]
RhOOH NSs/C-OH-40	1.0 M KOH	18 mV	[7]
Pt-AC/Cr−N−C	1.0 M KOH	19 mV	[8]
RhP_2/Rh@NPG	1.0 M KOH	21 mV	[9]
O–NiCu	1.0 M KOH	23 mV	[10]
Rh_2P CNs	1.0 M KOH	23 mV	[11]
Cu-doped Ru/$RuSe_2$ NSs/C	1.0 M KOH	29 mV	[12]
Pt-doped Rh metallene	1.0 M KOH	37 mV	[13]
Ni_xRh_{1-x}@200 °C	1.0 M NaOH	37 mV	[14]
Ni@IrNi	1.0 M KOH	33 mV	[15]
SA In-Pt NWs/C	1.0 M KOH	46 mV	[16]
RhP_x@NPC	1.0 M KOH	69 mV	[17]
8.2% Rh-$MoSe_2$	1.0 M KOH	73 mV	[18]
PtCu NF/C	1.0 M KOH	76 mV	[19]
$RhSe_2$	1.0 M KOH	82 mV	[20]
NMS/CC with Ni_3S_2/MoS_2 heterostructure	1.0 M KOH	146 mV	[21]

Table S3. Comparison of voltage needed for energy-saving H_2 production of RhNi NCs with other recently reported electrocatalysts at 10 mA cm^{-2}.

Catalysts	Electrolytes	Voltages of HER/EOR @ 10 mA cm^{-2}	References
RhNi NCs	1.0 M KOH || (1.0 M KOH + 1.0 M EtOH)	0.53 V	This work
	1.0 M KOH || (1.0 M KOH + 1.0 M MeOH)	0.58 V	This work
	1.0 M KOH || (1.0 M KOH + 1.0 M GLY)	0.46 V	This work
	1.0 M KOH || (1.0 M KOH + 1.0 M EG)	0.52 V	This work
PtCu NF/C	1.0 M KOH || (1.0 M KOH + 0.5 M EtOH)	0.58 V	[19]
SA In-Pt NWs/C	1.0 M KOH || (1.0 M KOH + 0.5 M EtOH)	0.62 V	[16]
Pd_2Ga/C	0.5 M KOH + 0.5 M EtOH	0.62 V	[22]
Pd_3Pb@2.9%Pt	1.0 M KOH + 1.0 M EtOH	0.75 V	[23]
RhNiFe-P NF	1.0 M KOH + 0.5 M EtOH	1.42 V	[24]
Co_3S_4-NSs/Ni-F	1.0 M KOH + 0.5 M EtOH	1.48 V	[25]
$CuCo_2S_4$/CC	1.0 M KOH + 1.0 M EtOH	1.59 V	[26]
Ni–MoN/NF-6	0.5 M H_2SO_4 || 1.0 M KOH + 0.5 M MeOH	0.56 V	[27]
Pt/$MoSe_2$@MHCS	0.5 M H_2SO_4 + 1.0 M MeOH	0.62 V	[28]
Pd@$Rh_{0.07}$Pd NDs	1.0 M KOH || (1.0 M KOH + 0.5 M MeOH)	0.81 V	[29]
NiIr-MOF/NF	1.0 M KOH || (1.0 M KOH + 4.0 M MeOH)	1.39 V	[30]
$Co(OH)_2$@HOS/CP	1.0 M KOH + 3.0 M MeOH	1.39 V	[31]
$Ni_{50}Co_{15}Fe_{30}Cu_5$ MEAAs	1.0 M KOH + 1.0 M MeOH	1.48 V	[32]
$Ni(OH)_2$/NF	1.0 M KOH + 0.5 M MeOH	1.52 V	[33]
Co-Rh_2	1.0 M KOH || (1.0 M KOH + 1.0 M MeOH)	1.55 V	[34]
(CoNiCuMnMo)Se/CF	0.5 M H_2SO_4 || (1.0 M KOH + 0.1 M GLY)	0.50 V	[35]
CoNiCuMnMo-NPs/CC	0.5 M H_2SO_4 || (1.0 M KOH + 0.1 M GLY)	~ 0.58 V	[36]
CuO@Co-MOF	1.0 M KOH || (1.0 M KOH + 0.1 M GLY)	~ 0.91 V	[37]
CuO/CF	1.0 M KOH || (1.0 M KOH + 0.1 M GLY)	~ 1.15 V	[38]
$NiCo_2O_4$/NF	1.0 M KOH + 0.1 M GLY	1.15 V	[39]

(Continued)

Catalysts	Electrolytes	Voltages of HER/EOR @ 10 mA cm^{-2}	References
Mn-Co-S/NF	1.0 M KOH + 0.3 M GLY	~ 1.32 V	[40]
NiVRu-LDHs NAs/NF	1.0 M KOH || (1.0 M KOH + 0.1 M GLY)	1.35 V	[41]
MnO$_2$/CP	0.005 M H$_2$SO$_4$ + 0.2 M GLY	1.36 V	[42]
RuCu-CAT/CF	1.0 M KOH || (1.0 M KOH + 0.5 M GLY)	1.36 V	[43]
Pt−Ni(OH)$_2$/NF	1.0 M KOH || (1.0 M KOH + 0.1 M EG)	~ 0.48 V	[44]
Pd-Ni(OH)$_2$/NF	1 M KOH + 1.0 M EG	0.52 V	[45]
Rh/RhOOH metallene	1.0 M KOH + 6.0 M EG	~ 0.66 V	[46]
Ru/Ni$_2$P/NF	1 M KOH + 0.5 M EG	1.14 V	[47]

3. References

[1] J. P. Perdew, K. Burke and M. Ernzerhof, *Phys. Rev. Lett.*, 1996, **77**, 3865–3868.

[2] G. Kresse and J. Hafner, *Phys. Rev. B*, 1993, **48**, 13115–13118.

[3] G. Kresse and D. Joubert, *Phys. Rev. B*, 1999, **59**, 1758–1775.

[4] P. E. Blöchl, *Phys. Rev. B*, 1994, **50**, 17953–17979.

[5] G. Mills, H. Jónsson and G. K. Schenter, *Surf. Sci.*, 1995, **324**, 305–337.

[6] X. M. Wang, G. F. Long, B. Liu, Z. L. Li, W. S. Gao, P. F. Zhang, H. Zhang, X. Zhou, R. Z. Duan, W. Hu and C. Li, *Angew. Chem. Int. Ed.*, 2023, **62**, e202301562.

[7] S. X. Bai, M. Xie, T. Cheng, K. L. Cao, Y. Xu and X. Q. Huang, *Nano Energy*, 2020, **78**, 105224.

[8] L. Y. Zeng, Z. L. Zhao, Q. Z. Huang, C. H. Zhou, W. X. Chen, K. Wang, M. G. Li, F. X. Lin, H. Luo, Y. Gu, L. Li, S. P. Zhang, F. Lv, G. Lu, M. C. Luo and S. J. Guo, *J. Am. Chem. Soc.*, 2023, **145**, 21432−21441.

[9] Y. H. Liu, J. Ding, F. H. Li, X. Z. Su, Q. T. Zhang, G. J. Guan, F. X. Hu, J. C. Zhang, Q. L. Wang, Y. C. Jiang, B. Liu and H. B. Yang, *Adv. Mater.*, 2023, **35**, 2207114.

[10] J. S. Wang, S. S. Xin, Y. Xiao, Z. F. Zhang, Z. M. Li, W. Zhang, C. J. Li, R. Bao, J. Peng, J. H. Yi and S. L. Chou, *Angew. Chem. Int. Ed.*, 2022, **61**, e202202518.

[11] S. F. Yang, X. B. Yang, Q. Wang, X. Q. Cui, H. B. Zou, X. L. Tong and N. J. Yang, *Chem. Eng. J.*, 2022, **449**, 137790.

[12] K. Wang, J. H. Zhou, M. Z. Sun, F. X. Lin, B. L. Huang, F. Lv, L. Y. Zeng, Q. H. Zhang, L. Gu, M. C. Luo and S. J. Guo, *Adv. Mater.*, 2023, **35**, 2300980.

[13] Q. Q. Mao, W. X. Wang, K. Deng, H. J. Yu, Z. Q. Wang, Y. Xu, X. N. Li, L. Wang and H. J. Wang, *J. Energy Chem.*, 2023, **85**, 58−66.

[14] D. Jin, A. Yu, Y. Lee, M. H. Kim and C. Lee, *J. Mater. Chem. A*, 2020, **8**, 8629–8637.

[15] J. Xu, X. Y. Wang, X. N. Mao, K. Feng, J. B. Xu, J. Zhong, L. Wang, N. Han and Y. G. Li, *Energy Environ. Sci.*, 2023, **16**, 6120–6126.

[16] Y. M. Zhu, X. R. Zhu, L. Z. Bu, Q. S, Y. F. Li, Z. W. Hu, C.-T. Chen, C.-W. Pao, S. Z. Yang and X. Q. Huang, *Adv. Funct. Mater.*, 2020, **30**, 2004310.

[17] J.-Q. Chi, X.-J. Zeng, X. Shang, B. Dong, Y.-M. Chai, C.-G. Liu, M. Marin and Y. D. Yin, *Adv. Funct. Mater.*, 2019, **29**, 1901790.

[18] Y. M. Zhao, C. L. Yang, G. X. Mao, J. Su, G. Z. Cheng and W. Luo, *Inorg. Chem. Front.*, 2018, **5**, 2978–2984.

[19] H. Fu, N. Zhang, F. L. Lai, L. S. Zhang, S. L. Chen, H. J. Li, K. Z. Jiang, T. Zhu, F. P. Xu and T. X. Liu, *ACS Catal.*, 2022, **12**, 11402−11411.

[20] W. W. Zhong, B. B. Xiao, Z. P. Lin, Z. P. Wang, L. G. Huang, S. J. Shen, Q. H. Zhang and L. G, *Adv. Mater.*, 2021, **33**, 2007894.

[21] L. Y. Zhang, Y. J. Zheng, J. C. Wang, Y. Geng, B. Zhang, J. J. He, J. M. Xue, T. Frauenheim and M. Li, *Small*, 2021, **17**, 2006730.

[22] Q. X. Wang, J. F. Liu, T. Li, T. Zhang, J. Arbiolb, S. X. Yan, Y. Wang, H. M. Li and A. Cabot, *Chem. Eng. J.*, 2022, **446**, 136878.

[23] T. Li, Q. X. Wang, J. J. Wu, Y. P. Sui, P. Y. Tang, H. T. Liu, W. J. Zhang, H. M. Li, Y. Wang, A. Cabot and J. F. Liu, *Small*, 2023, **20**, 2306178.

[24] J. Miao, X. J. Zhao, H.-Y. Hu, H. Huang, Y. Ding, Z.-H. Liu and Y. Chen, *ACS Appl. Nano Mater.*, 2022, **5**, 4948−4957.

[25] Y. Ding, Q. Xue, Q.-L. Hong, F.-M. Li, Y.-C. Jiang, S.-N. Li and Y. Chen, *ACS Appl. Mater. Interfaces*, 2021, **13**, 4026−4033.

[26] S. Sheng, K. Ye, Y. Y. Gao, K. Zhu, J. Yan, G. L. Wang and D. X. Cao, *J. Colloid Interface Sci.*, 2021, **602**, 325–333.

[27] C. M. Rao, H. J. Wang, K. Chen, H. Y. Chen, S. Q. Ci, Q. H. Xu and Z. H. Wen, *Small*, 2024, **20**, 2303300.

[28] F. L. Yang, W. Qiao, L. C. Yu, S. L. Wang and L. G. Feng, *Chem. Eng. J.*, 2024, **483**, 149055.

[29] Y.-C. Jiang, H.-Y. Sun, Y.-N. Li, J.-W. He, Q. Xue, X. L. Tian, F.-M. Li, S.-B. Yin, D.-S. Li and Y. Chen, *ACS Appl.*

Mater. Interfaces, 2021, **13**, 35767−35776.

[30] Y. Xu, M. Y. Liu, M. Z. Wang, T. L. Ren, K. L. Ren, Z. Q. Wang, X. N. Li, L. Wang and H. J. Wang, *Appl. Catal., B*, 2022, **300**, 120753.

[31] K. Xiang, D. Wu, X. H. Deng, M. Li, S. Y. Chen, P. P. Hao, X. F. Guo, J.-L. Luo and X.-Z. Fu, *Adv. Funct. Mater.*, 2020, **30**, 1909610.

[32] G. H. Han, M. G. Li, H. Liu, W. Y. Zhang, L. He, F. Y. Tian, Y. Q. Liu, Y. S. Yu, W. W. Yang and S. J. Guo, *Adv. Mater.*, 2022, **34**, 2202943.

[33] J. Hao, J. W. Liu, D. Wu, M. X. Chen, Y. Liang, Q. Wang, L. Wang, X.-Z. Fu and J.-L. Luo, *Appl. Catal., B*, 2021, **281**, 119510.

[34] Y. Guo, X. B. Yang, X. C. Liu, X. L. Tong and N. J. Yang, *Adv. Funct. Mater.*, 2023, **33**, 2209134.

[35] H. Yao, Y. B. Wang, Y. N. Zheng, X. Yu, J. J. Ge, Y. H. Zhu and X. H. Guo, *Nano Res.*, 2023, **16**, 10832−10839.

[36] L. F. Fan, Y. X. Ji, G. X. Wang, J. X. Chen, K. Chen, X. Liu and Z. H. Wen, *J. Am. Chem. Soc.*, 2022, **144**, 7224−7235.

[37] Z. F. Zhao, X. Y. Shen, X. Y. Luo, M. H. Chen, M. D. Zhang, R. P. Yu, R. T. Jin and H. J. Zheng, *Adv. Energy Mater.*, 2024, **14**, 2400851.

[38] R.-Y. Fan, X.-J. Zhai, W.-Z. Qiao, Y.-S. Zhang, N. Yu, N. Xu, Q.-X. Lv, Y.-M. Chai and B. Dong, *Nano-Micro Lett.*, 2023, **15**, 190.

[39] W. S. Luo, H. Tian, Q. Li, G. Meng, Z. W. Chang, C. Chen, R. X. Shen, X. Yu, L. B. Zhu, F. T. Kong, X. Z. Cui and J. L. Shi, *Adv. Funct. Mater.*, 2024, **34**, 2306995.

[40] Y. Fang, C. F. Dai, X. Y. Liu, Y. X. Wang, C. Ju, S. J. He, R. Shi, Y. N. Liu, J. G. Zhang, Y. F. Zhu and J. Wang, *Nano Energy*, 2024, **127**, 109754.

[41] Q. Z. Qian, X. Y. He, Z. Y. Li, Y. X. Chen, Y. F. Feng, M. Y. Cheng, H. K. Zhang, W. T. Wang, C. Xiao, G. Q. Zhang and Y. Xie, *Adv. Mater.*, 2023, **35**, 2300935.

[42] Y. Li, X. F. Wei, S. .H. Han, L. S. Chen and J. L. Shi, *Angew. Chem., Int. Ed.*, 2021, **60**, 21464–21472.

[43] Y. Q. He, Z. Ma, F. Yan, C. L. Zhu, T. Y. Shen, S. L. Chou, X. Zhang and Y. J. Chen, *PNAS*, 2024, **121**, e2320777121.

[44] X. Liu, X. Y. He, D. K. Xiong, G. Y. Wang, Z. T. Tu, D. L. Wu, J. Y. Wang, J. Gu and Z. F. Chen, *ACS Catal.*, 2024, **14**, 5366−5376.

[45] F. L. Liu, X. T. Gao, R. Shi, Z. X. Guo, E. C. M. Tse and Y. Chen, *Angew. Chem., Int. Ed.*, 2023, **62**, e202300094.

[46] Q. Q. Mao, K. Deng, H. J. Yu, Y. Xu, Z. Q. Wang, X. N. Li, L. Wang and H. J. Wang, *Adv. Funct. Mater.*, 2022, **32**, 2201081.

[47] G. Ma, N. Yang, Y. F. Xue, G. F. Zhou and X. Wang, *ACS Appl. Mater. Interfaces*, 2021, **13**, 42763−42772.